Microwave graph analogs for the voltage drop in three-terminal devices with orthogonal, unitary, and symplectic symmetry

F. Castañeda-Ramírez,[1] A. M. Martínez-Argüello,[2,*] T. Hofmann,[3] A. Rehemanjiang,[3]
M. Martínez-Mares,[1] J. A. Méndez-Bermúdez,[4] U. Kuhl,[5] and H.-J. Stöckmann[3]

[1]*Departamento de Física, Universidad Autónoma Metropolitana-Iztapalapa, Apartado Postal 55-534, 09340 Ciudad de México, Mexico*
[2]*Instituto de Ciencias Físicas, Universidad Nacional Autónoma de México, Apartado Postal 48-3, 62210 Cuernavaca, Morelos, Mexico*
[3]*Fachbereich Physik der Philipps–Universität Marburg, D-35032 Marburg, Germany*
[4]*Instituto de Física, Benemérita Universidad Autónoma de Puebla, Apartado Postal J-48, 72570 Puebla, Puebla, Mexico*
[5]*Université Côte d'Azur, CNRS, Institut de Physique de Nice (INPHYNI), 06108 Nice, France*

(Received 28 June 2021; revised 1 October 2021; accepted 21 December 2021; published 4 January 2022)

Transmission measurements through three-port microwave graphs are performed, in analogy to three-terminal voltage drop devices with orthogonal, unitary, and symplectic symmetry. The terminal used as a probe is symmetrically located between two chaotic subgraphs, and each graph is connected to one port, the input and the output, respectively. The analysis of the experimental data clearly exhibits the weak localization and antilocalization phenomena. We find a good agreement with theoretical predictions, provided that the effects of dissipation and imperfect coupling to the ports are taken into account.

DOI: 10.1103/PhysRevE.105.014202

I. INTRODUCTION

The wave origin of quantum interference in many physical phenomena opens the possibility that analogous classical wave systems may emulate quantum devices [1]. For example, classical wave systems have been used as auxiliary tools to understand transport properties of multiterminal quantum systems. The dissipation that occurs in classical wave systems and the imperfect coupling to the leads that feed the system have not been disadvantageous but interesting phenomena deserving to be studied to analyze their effects in transport properties [2–5].

An opportunity to study many electrical or thermal conduction properties of solid state physics by classical wave systems has been opened once the problem of electrical or thermal conduction is reduced to a scattering problem. For instance, the Landauer formula states that the electrical conductance is proportional to the transmission coefficient [6]; an equivalent Landauer formula is valid for thermal conductance [7]. Therefore, much research has been devoted to the study of conduction through two-terminal configurations from the theoretical and experimental points of view, using quantum mechanics [8–12] as well as classical wave physics [2,3,13,14].

Electrical conduction through multiterminal quantum devices has also been studied in [15–23]. Among them three-terminal systems have been considered in which the voltage drop along the system is another observable of interest [24–27], apart from the conductance coefficients. While two of the terminals are connected to fixed electronic reservoirs to feed the system, the third one is used as a probe that tunes the voltage drop. The voltage drop along a disordered wire was analyzed for the one-channel case [25,26]. It has been shown theoretically that the value of the voltage drop lies between those on the two terminals; in fact, it consists of the average of the voltages in the terminals and a deviation term, which contains specific information about the system through the transmission coefficients from the terminals to the probe. This dimensionless voltage drop deviation term, f, is an important quantity in the study of the voltage drop reducing the problem to a scattering problem. It has been shown that f fluctuates from sample to sample, and its statistical distribution has a completely different shape for metallic and insulating regimes [25,26]. The same quantity was also considered for a chaotic system, numerically simulated using random matrix theory (RMT) [27].

Again, once the problem of electrical conduction is reduced to a scattering problem, classical wave systems may help in the understanding of the voltage drop along a quantum resistor. More recently, an experiment with microwave graphs has been performed for an asymmetric configuration, where the probe is located on one side of a chaotic graph [28]. Analytical and numerical procedures were carried out to compute f. Remarkably, the results show significant differences with respect to the corresponding disordered case. Here we deepen the understanding of the voltage drop by proposing an experiment with microwave graphs but locating the probe between two chaotic graphs, as shown in Fig. 1, that is, in a symmetric configuration. Our proposal is accompanied by analytical predictions.

The paper is organized as follows. In the next section we obtain the analytical expressions for the voltage drop for a measurement at the middle of two scattering devices. It is written in terms of the scattering matrices of the individual devices. In Sec. III the analytical procedure, using

*blitzkriegheinkel@gmail.com

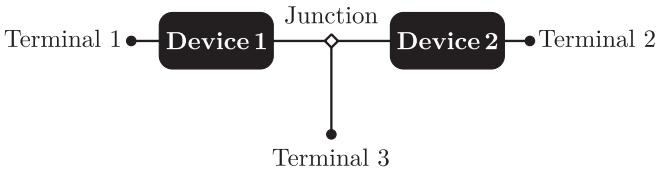

FIG. 1. Schematic representation of the three-terminal system for measuring the voltage drop in a symmetric configuration through the third terminal located between two chaotic devices.

RMT calculations for the scattering matrices, is developed for the statistical distribution of the deviation f assuming chaotic scattering devices. The experimental realization with microwave graphs is explained in Sec. IV, where we compare experimental results with theoretical predictions. Finally, we present our conclusions in Sec. V.

II. VOLTAGE DROP REDUCED TO A SCATTERING PROBLEM

A. Voltage drop in a symmetric configuration of measurement

To measure the voltage drop along a quantum wire in the simplest configuration, a three-terminal system is needed in which one of the ports is used as a probe by tuning its voltage to zero current. By symmetric configuration of measurement we mean the one in which the probe is located between two quantum devices, as is schematically shown in Fig. 1. In the experiment the two devices are realized in terms of microwave graphs belonging to the same symmetry class with the same mean density of states, i.e., the same total length but different geometries. We are interested in the one-channel situation of the leads connecting the system, for which the zero current in the probe implies that [6]

$$\mu_3 = \tfrac{1}{2}(\mu_1 + \mu_2) + \tfrac{1}{2}(\mu_1 - \mu_2)\, f, \tag{1}$$

where μ_i is the chemical potential of the ith electronic reservoir and

$$f = \frac{T_{31} - T_{32}}{T_{31} + T_{32}}, \tag{2}$$

with T_{ij} the transmission coefficient from terminal j to terminal i. Equation (1) is appealing since it allows us to discriminate the part of the voltage drop that comes from the fixed potentials, μ_1 and μ_2, and the one that comes from the scattering process in the system. For instance, if the two devices are clean (free of impurities) straight waveguides, $T_{31} = T_{32}$, such that $f = 0$ and μ_3 reduces to the average value between μ_1 and μ_2. But, if $T_{32} = 0$, which means that device 2 is blocked, $f = 1$ and μ_3 becomes equal to μ_1. On the other hand, if device 1 is blocked, $T_{31} = 0$ and $f = -1$, in which case $\mu_3 = \mu_2$. In general, f takes values in the interval $[-1, 1]$ and says to which of the fixed potentials μ_3 is closer; its expression in Eq. (2) resembles that of the degree of polarization of light [29, p. 211, Eq. (6.40)]. Therefore, we will refer to f as the dimensionless voltage drop deviation.

B. Voltage drop deviation f in terms of scattering elements

Since the voltage drop is an observable in electrical conduction, it has no meaning in classical wave systems, but it can be addressed through the quantity f indirectly. Equation (2) is equivalent to the dimensionless conductance but for three-terminal devices. Analogously to the conductance, the problem of the voltage drop in electronic devices is reduced to a scattering problem through the quantity f. It is clear that f contains all the information about the system by means of the transmission coefficients T_{ij}. Let us assume that the scattering properties of each device are known through their scattering matrices, S_1 for device 1 and S_2 for device 2. The general structure of these matrices depends on the symmetry properties of the problem, namely,

$$S_j = \begin{pmatrix} r_j J & t'_j D_j \\ t_j D_j^R & r'_j J \end{pmatrix}, \quad j = 1,\ 2, \tag{3}$$

where r_j (r'_j) and t_j (t'_j) are the reflection and transmission amplitudes for incidence from the left (right) of device j. Unitarity is the only requirement on S_j in absence of any symmetry; this case is known as the unitary symmetry and is labeled by $\beta = 2$ in Dyson's scheme. In addition, in the presence of time reversal invariance S_j is unitary and symmetric, which corresponds to the orthogonal symmetry and is labeled by $\beta = 1$; for both cases $D_j = D_j^R = J = 1$. Furthermore, in the presence of time-reversal invariance but no spin-rotation symmetry, the symmetry of the system is the symplectic one, labeled by $\beta = 4$, and S_j becomes a 4×4 self-dual matrix [30] in which case J is the 2×2 identity matrix, $J = \mathbb{1}$, and D_j^R is the dual matrix of the 2×2 matrix D_j, defined by [31]

$$D_j^R = -Z D_j^T Z, \tag{4}$$

where

$$Z = \begin{pmatrix} 0 & -1 \\ 1 & 0 \end{pmatrix}, \tag{5}$$

and D_j^T is the transposed matrix of D_j with the form $D_j = U_j V_j^R$, where V_j^R is the dual of V_j, with U_j and V_j being 2×2 matrices that belong to the SU(2) group.

The dependence of T_{ij} on S_1 and S_2 can be obtained explicitly. The scattering matrix of the three-terminal symmetric configuration is given by [27]

$$\mathbf{S} = S_{PP} + S_{PQ}(S_0 - S_{QQ})^{-1} S_{QP}, \tag{6}$$

where S_0 is the scattering matrix of the junction that accounts for the coupling to the probe. In fact, S_0 can be obtained from the experiment [28,32]; it reads as

$$S_0 = \frac{1}{3}\begin{pmatrix} -J & 2J & 2J \\ 2J & -J & 2J \\ 2J & 2J & -J \end{pmatrix}. \tag{7}$$

In Eq. (6) S_{PP} represents the reflections to the terminals, and S_{QP} and S_{PQ} represent the transmissions from the terminals to the inner part of the system and from the inner part to the terminals; S_{QQ} represents the internal reflections and $(S_0 - S_{QQ})^{-1}$ accounts for the multiple scattering between the

devices and the junction. Explicitly, they are

$$S_{PP} = \begin{pmatrix} r_1 J & 0 & 0 \\ 0 & r_2' J & 0 \\ 0 & 0 & 0 \end{pmatrix}, \quad S_{PQ} = \begin{pmatrix} t_1' D_1 & 0 & 0 \\ 0 & t_2 D_2^R & 0 \\ 0 & 0 & J \end{pmatrix},$$
$$S_{QP} = \begin{pmatrix} t_1 D_1^R & 0 & 0 \\ 0 & t_2' D_2 & 0 \\ 0 & 0 & J \end{pmatrix}, \quad S_{QQ} = \begin{pmatrix} r_1' J & 0 & 0 \\ 0 & r_2 J & 0 \\ 0 & 0 & 0 \end{pmatrix}. \tag{8}$$

By substituting Eqs. (7) and (8) into Eq. (6), the scattering matrix elements $\mathbf{S}_{31}$ and $\mathbf{S}_{32}$ are obtained, from which $T_{ij} = |\mathbf{S}_{ij}|^2$ for $\beta = 1,\ 2$, while $T_{ij} = \frac{1}{2}\mathrm{tr}(\mathbf{S}_{ij}\mathbf{S}_{ij}^\dagger)$ for $\beta = 4$, and therefore Eq. (2) reduces to

$$f = \frac{|t_1|^2|1 + r_2|^2 - |t_2'|^2|1 + r_1'|^2}{|t_1|^2|1 + r_2|^2 + |t_2'|^2|1 + r_1'|^2}. \tag{9}$$

Note that S_{31}, S_{32}, and f depend only on the elements of the individual scattering matrices that describe the devices.

III. CHAOTIC SCATTERING FOR THE VOLTAGE DROP DEVIATION

Of particular interest are the transport properties through chaotic devices, quantum or classical. The disordered three-terminal system was previously considered in Ref. [26]. In any case the scattering quantities, like the transmission coefficients through each device, fluctuate with respect to a tuning parameter, like the energy of the incident particles in the quantum case or the frequency in the classical wave situation, or from sample to sample. Therefore, it is the distribution of f that becomes more important rather than a particular value of f.

For a chaotic cavity, the statistical fluctuations of the scattering matrix are described by RMT. There S_j is uniformly distributed according to the invariant measure $d\mu_\beta(S_j)$ that defines the circular ensemble for the symmetry class β: the circular orthogonal ensemble for $\beta = 1$, the circular unitary ensemble for $\beta = 2$, and the circular symplectic ensemble for $\beta = 4$. Hence, the statistical distribution of f can be calculated from the definition

$$P_\beta(f) = \int \delta\Big(f - \frac{T_{31} - T_{32}}{T_{31} + T_{32}}\Big) d\mu_\beta(S_1)\, d\mu_\beta(S_2), \tag{10}$$

where δ is the Dirac delta function.

A. Statistical distribution of the voltage drop deviation f

A useful parametrization for scattering matrices is the polar form

$$S_j = \begin{bmatrix} -\sqrt{1-\tau_j}\, e^{i(\phi_j + \phi_j')} J & \sqrt{\tau_j}\, e^{i(\phi_j + \psi_j')} D_j \\ \sqrt{\tau_j}\, e^{i(\psi_j + \phi_j')} D_j^R & \sqrt{1-\tau_j}\, e^{i(\psi_j + \psi_j')} J \end{bmatrix}, \tag{11}$$

where $0 \leqslant \tau_j \leqslant 1$ and ϕ_j, ϕ_j', ψ_j, ψ_j' lie in the interval $[0,\ 2\pi]$; $\phi_j = \phi_j'$ and $\psi_j = \psi_j'$ for $\beta = 1,\ 4$, and J, D_j, and D_j^R are as defined in Sec. II B.

For this parametrization, the normalized invariant measure of S_j is given by

$$d\mu_\beta(S_j) = p_\beta(\tau_j)\, d\tau_j\, \frac{d\phi_j}{2\pi}\, \frac{d\psi_j}{2\pi} \times \begin{cases} 1 & \text{for} \quad \beta = 1 \\ \frac{d\phi_j'}{2\pi}\, \frac{d\psi_j'}{2\pi} & \text{for} \quad \beta = 2 \\ d\mu(U_j)\, d\mu(V_j) & \text{for} \quad \beta = 4 \end{cases}, \quad \text{where} \quad p_\beta(\tau_j) = \frac{\beta}{2}\tau_j^{\beta/2-1} \tag{12}$$

and $d\mu(U_j)$ and $d\mu(V_j)$ are the invariant measures of U_j and V_j, respectively. As we will see below, f does depend on neither U_j nor V_j such that we do not need to know explicitly the expressions for $d\mu(U_j)$ and $d\mu(V_j)$.

In terms of the parametrization of Eq. (11) the voltage drop deviation, given in Eq. (9), can be written as

$$f = 1 + \frac{\tau_1\tau_2 - 2\tau_2 - 2\tau_2\sqrt{1-\tau_1}\cos(\psi_1 + \psi_1')}{\tau_1 + \tau_2 - \tau_1\tau_2 - \tau_1\sqrt{1-\tau_2}\cos(\phi_2 + \phi_2') + \tau_2\sqrt{1-\tau_1}\cos(\psi_1 + \psi_1')}. \tag{13}$$

Since f does not depend on either U_j or V_j, the integration over $d\mu(U_j)$ and $d\mu(V_j)$ in Eq. (10) gives just 1 for $\beta = 4$; except for variables τ_1 and τ_2, the resulting expression for $P_\beta(f)$ reduces to one similar to that for $\beta = 1$ in the remaining variables. The integration of $d\phi_1/2\pi$, $d\phi_1'/2\pi$, $d\psi_2/2\pi$, and $d\psi_2'/2\pi$ gives 1 for $\beta = 2$. Therefore, once we perform the integration with respect to ϕ_2 and ϕ_2', making the appropriate change of variables for each symmetry class, and then with respect to the remaining phases ψ_1 and ψ_1', we arrive at

$$P_\beta(f) = \int_0^1 d\tau_1 \int_0^1 d\tau_2\, p_\beta(\tau_1)\, p_\beta(\tau_2)\, p(f|\tau_1, \tau_2), \tag{14}$$

where $p(f|\tau_1, \tau_2)$ can be interpreted as the conditional probability distribution of f given τ_1 and τ_2, and it is given by

$$p(f|\tau_1, \tau_1) = \frac{1}{\pi^2(1-f^2)\sqrt{1-\tau_1}} \int_L \frac{2 - \tau_1 + 2\sqrt{1-\tau_1}\, x}{\sqrt{(\alpha_+ - x)(x - \alpha_-)(1-x^2)}}\, dx, \tag{15}$$

where $L \in (-1,\ 1) \cap (\alpha_-, \alpha_+)$ with

$$\alpha_\pm = \frac{(\tau_1 - \tau_2) - (\tau_1 + \tau_2 - \tau_1\tau_2)f \pm (1-f)\tau_1\sqrt{1-\tau_2}}{(1+f)\tau_2\sqrt{1-\tau_1}}. \tag{16}$$

The integration in the domain L is not a trivial problem because it depends on the variables τ_1, τ_2, and f through $\alpha_\pm$ in a complicated way, but we can give a further step in the integration by looking for the limits of integration once the value of f is fixed (see Appendix A for details). The integral over x in Eq. (15) can be expressed in terms of complete elliptic integrals. The result for $P_\beta(f)$ can be expressed as

$$P_\beta(f) = \frac{1}{\pi^2(1-f^2)}\Bigg[\int_0^1 d\tau_1 \frac{p_\beta(\tau_1)}{\sqrt{1-\tau_1}} \int_0^{u(\tau_1)} d\tau_2\, p_\beta(\tau_2)\, I^1_{-1}(f;\tau_1,\tau_2) + \int_0^1 d\tau_2\, p_\beta(\tau_2) \int_0^{w(\tau_2)} d\tau_1 \frac{p_\beta(\tau_1)}{\sqrt{1-\tau_1}}\, I^{\alpha_+}_{\alpha_-}(f;\tau_1,\tau_2)$$
$$+ H(f)\,H(1-f) \int_0^1 d\tau_1 \frac{p_\beta(\tau_1)}{\sqrt{1-\tau_1}} \int_{u(\tau_1)}^{v(\tau_1)} d\tau_2\, p_\beta(\tau_2)\, I^{\alpha_+}_{-1}(f;\tau_1,\tau_2) + H(-f)\,H(f+1) \int_0^1 d\tau_1 \frac{p_\beta(\tau_1)}{\sqrt{1-\tau_1}}$$
$$\times \int_{u(\tau_1)}^{v(\tau_1)} d\tau_2\, p_\beta(\tau_2)\, I^1_{\alpha_-}(f;\tau_1,\tau_2)\Bigg], \tag{17}$$

where $H(x)$ is the Heaviside step function and the limits are

$$u(\tau_1) = \frac{r(2s_- - r)}{s_-^2}, \quad v(\tau_1) = \frac{r(2s_+ - r)}{s_+^2}, \quad \text{and} \quad w(\tau_2) = \frac{r'(2s' - r')}{s'^2}, \tag{18}$$

where $r' = r(\tau_1 \to \tau_2)$ and $s' = s_-(\tau_1 \to \tau_2)$ with

$$r(\tau_1) = (1-f)\tau_1 \quad \text{and} \quad s_\pm(\tau_1) = 1 + (1-\tau_1)f \pm (1+f)\sqrt{1-\tau_1}. \tag{19}$$

In Eq. (17),

$$I^1_{-1}(f;\tau_1,\tau_2) = \frac{2}{\sqrt{(\alpha_+ + 1)(1-\alpha_-)}}\Big[(A + B\alpha_-)K(k_1) - (1+\alpha_-)B\,\Pi\big(r_1^2, k_1\big)\Big], \tag{20}$$

$$I^{\alpha_+}_{\alpha_-}(f;\tau_1,\tau_2) = \frac{2}{\sqrt{(\alpha_+ + 1)(1-\alpha_-)}}\Big[(A - B)K(k_1) + (1+\alpha_-)B\,\Pi\big(r_1'^2, k_1\big)\Big], \tag{21}$$

$$I^{\alpha_+}_{-1}(f;\tau_1,\tau_2) = \frac{\sqrt{2}}{\sqrt{\alpha_+ - \alpha_-}}\Big[(A + B\alpha_-)K(k_2) - (1+\alpha_-)B\,\Pi\big(r_2'^2, k_2\big)\Big], \tag{22}$$

and

$$I^1_{\alpha_-}(f;\tau_1,\tau_2) = \frac{\sqrt{2}}{\sqrt{\alpha_+ - \alpha_-}}\Big[(A - B)K(k_2) + (1+\alpha_-)B\,\Pi\big(r_2^2, k_2\big)\Big], \tag{23}$$

where $A = 2 - \tau_1$ and $B = 2\sqrt{1-\tau_1}$; $K(k)$ and $\Pi(r^2, k)$ are complete elliptic integrals of the first and third kinds, respectively, and

$$k_1^2 = \frac{2(\alpha_+ - \alpha_-)}{(\alpha_+ + 1)(1-\alpha_-)}, \quad r_1^2 = \frac{2}{1-\alpha_-}, \quad \text{and} \quad r_1'^2 = \frac{\alpha_+ - \alpha_-}{\alpha_+ + 1}; \tag{24}$$

$$k_2^2 = \frac{1}{k_1^2}, \quad r_2^2 = \frac{1}{r_1^2}, \quad \text{and} \quad r_2'^2 = \frac{1}{r_1'^2}. \tag{25}$$

The remaining integrals with respect to τ_1 and τ_2 can be performed numerically. In order to verify our results, in Fig. 2 we compare them with the statistical distributions obtained from numerical simulations using Eqs. (11)–(13). An excellent agreement is observed.

We can observe in Fig. 2 that the distribution of f is symmetric with respect to $f = 0$, which is due to the symmetric configuration of measurement. Moreover, it diverges at $f = \pm 1$ for $\beta = 1$, a clear effect of the weak localization that does not occur for $\beta = 2$, which shows finite peaks at $f = \pm 1$. For $\beta = 4$ the distribution becomes zero at $f = \pm 1$ due to the weak antilocalization phenomenon. Each of these effects is better understood from Eq. (9), which captures the symmetry properties of the conductance of each device. The differences found in the $P_\beta(f)$ between the symmetry classes are important signatures of the chaotic setup we consider here since in the equivalent disordered configuration no differences were found [26].

IV. EXPERIMENTAL REALIZATIONS WITH MICROWAVE GRAPHS

Since the voltage drop deviation depends only on the scattering properties of the devices, it can be emulated in classical wave systems. To experimentally realize devices 1 and 2, we use microwave graphs. Since the seminal paper by Kottos and Smilansky [34] it has been well known that the statistical properties of eigenvalues for closed graphs as well as their scattering properties for open graphs can be described by RMT and the effective Hamiltonian approach if the quantum graphs are sufficiently "complex" [35–37]. Microwave networks have been proven to be an excellent experimental playground starting with a first realization of the Gaussian orthogonal ensemble (GOE) [38,39] as well as realizing the unitary (GUE) [40,41] and symplectic ensembles (GSE) [32,33]. Even though deviations from RMT predictions in small graphs are known, they contribute mainly to

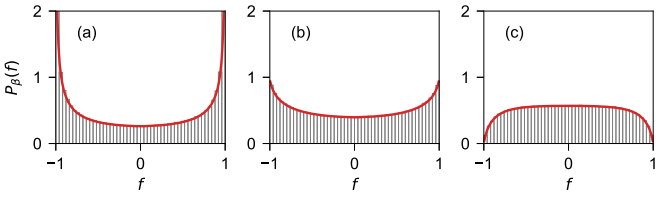

FIG. 2. Comparison between the analytical results (continuous lines) with random matrix simulations (histograms) for $P_\beta(f)$: (a) $\beta = 1$, (b) $\beta = 2$, and (c) $\beta = 4$.

long-range correlations [42] and have only small effects on the transmissions. Thus microwave networks give us the possibility to realize all three ensembles (GOE, GUE, GSE) and investigate experimentally the voltage drop deviation f. Another experimental realization for the orthogonal case based on microwave cavities (chaotic wave billiard) is given in Appendix B.

Figure 3(a) shows a photograph of the experimental setup for the case of time-reversal invariance ($\beta = 1$). The devices consist of chaotic microwave networks formed by coaxial semirigid cables (Huber & Suhner EZ-141) with SMA connectors, coupled by T junctions at the nodes. One microwave

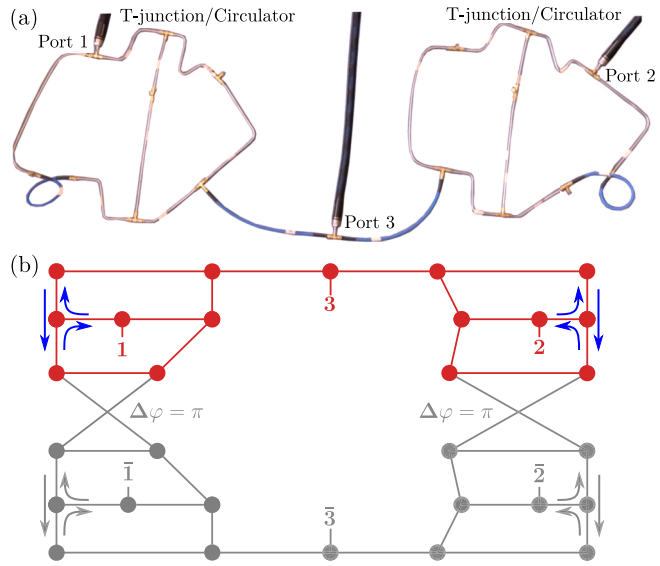

FIG. 3. (a) Photograph of the three-port experimental setup for the case of time-reversal symmetry ($\beta = 1$). For the realization of a violation of time-reversal symmetry ($\beta = 2$) one T junction in each of the subgraphs is replaced by a circulator. Both subgraphs are geometrically different but have the same total length, i. e., the mean level density is the same. (b) Sketch of the graph for $\beta = 1$ (GOE) and $\beta = 2$ (GUE), where for $\beta = 1$ the circulators are replaced by ordinary T junctions (indicated by the blue arrows). For a realization of $\beta = 4$ (GSE) each GUE subgraph is complemented by another geometrically identical one but with an opposite sense of rotation of the circulators (gray). The two respective copies are connected by pairs of bonds with length differences corresponding to a phase difference of π for the propagating waves (see Refs. [32,33] for details, where also a photograph of a single GSE graph can be found). The photograph shown in (a) corresponds to the graph sketched in red.

port attached to the left subgraph acts as the input, another one on the right as the output, and a third port attached to the connecting cable between the two subgraphs as the probe. To implement the violation of time-reversal invariance ($\beta = 2$), in each of the two subgraphs one of the T junctions is replaced by a circulator (Aerotek I70-1FFF) with an operating frequency range from 6 to 12 GHz. A circulator introduces directionality, waves entering via port 1 leave via port 2. The transmission intensities T_{31} and T_{32} were measured by an Agilent 8720ES vector network analyzer (VNA).

For the realization of the $\beta = 4$ (GSE) case two GSE graphs are needed. Since each GSE graph is composed of two GUE subgraphs, representing the spin-up and spin-down components [33], we need a total of four subgraphs. Figure 3(b) shows a sketch of the three-terminal GSE graph used to measure the scattering matrix. An essential ingredient of the setup is two pairs of bonds with length differences Δl corresponding to phase differences of $\Delta\varphi = \pi$ for the propagating waves. In the experiment we took many spectra for fixed Δl, which can be realized using phase shifters allowing one to change the length of one connecting bond automatically. Now the condition for the GSE symmetry of $\Delta\varphi = \pi$ is fulfilled only at specific Δl and k values, where k is the wave number. Therefore, we rescaled the spectra taken for constant Δl to new spectra for $\Delta\varphi$ constant, using $\Delta\varphi = k\Delta l$, and chose for the GSE realization the spectra where $\Delta\varphi = \pi$. Further details can be found in Refs. [32,33]. The ports now appear in pairs $1, \bar{1}, 2, \bar{2}, 3, \bar{3}$, and the scattering matrix elements turn into 2×2 matrices

$$\mathbf{S}_{ij} = \begin{pmatrix} S_{ij} & S_{i\bar{j}} \\ S_{\bar{i}j} & S_{\bar{i}\bar{j}} \end{pmatrix}. \tag{26}$$

In the spirit of the spin analogy, S_{ij} and $S_{i\bar{j}}$ correspond to transmissions without and with spin flip, respectively. $\mathbf{S}_{ij}$ can be written in terms of quaternions as $\mathbf{S}_{ij} = S^0_{ij}\mathbb{1} + \mathrm{i}S^x_{ij}\sigma_x + \mathrm{i}S^y_{ij}\sigma_y + \mathrm{i}S^z_{ij}\sigma_z$, where for a symplectic symmetry all coefficients S^0_{ij}, S^x_{ij}, etc., are real numbers and σ_j is the corresponding Pauli matrix j. As a consequence $\mathbf{S}_{ij}\mathbf{S}^\dagger_{ij}$ is a multiple of the unit matrix which allows for a simple check of the quality of the realization of the setup with symplectic symmetry. In our experiments $\mathbf{S}_{31}$ and $\mathbf{S}_{32}$ were found to be quaternion real within an error of 4.10% and 3.61%, respectively. The mentioned multiple is nothing but the transmission coefficient, hence $T_{31} = \frac{1}{2}\mathrm{tr}(\mathbf{S}_{31}\mathbf{S}^\dagger_{31})$ and $T_{32} = \frac{1}{2}\mathrm{tr}(\mathbf{S}_{32}\mathbf{S}^\dagger_{32})$.

The experimental distribution of f is shown in Fig. 4 as histograms for the three symmetry classes β, where it is compared with the theoretical result given by Eq. (17). As can be observed there is a qualitatively good agreement for all β. Despite the fact that there is a quantitative difference between theory and experiment, which is due to the phenomena of dissipation and imperfect coupling between the graphs and ports, this difference is not so large. In Fig. 4 we also show the corrected distributions obtained from RMT simulations, using the Heidelberg approach (see below), once these two phenomena, dissipation and imperfect coupling, are taken into account.

The dissipation and imperfect coupling can be quantified by two parameters: T_1 for the coupling strength and γ for the dissipation. The coupling between the graphs and ports T_1

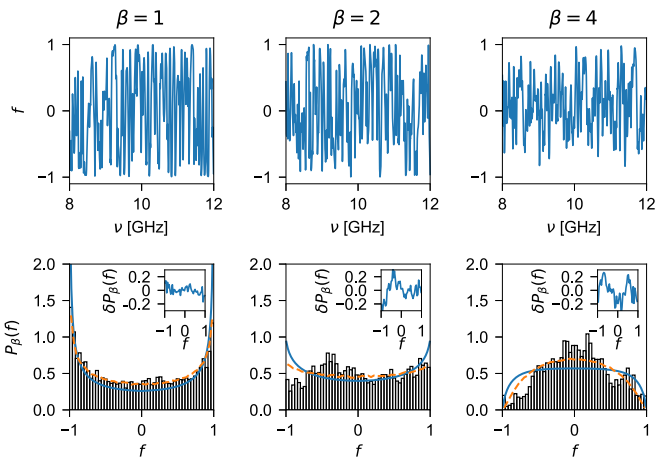

FIG. 4. Experimental voltage drop deviation f as a function of frequency is shown in the upper panels for the three symmetry classes. Their corresponding statistical distributions are shown as histograms. The continuous (blue) lines in the lower panels correspond to the theoretical result shown in Fig. 2, while the dashed (orange) lines are the RMT simulations which take into account the dissipation and imperfect coupling: $\beta = 1$ (left), $\beta = 2$ (middle), and $\beta = 4$ (right). For comparison purposes, in the insets in the lower panels we show the difference between the numerical and the experimental distribution $\delta P_\beta(f) = P_\beta(f)_{\rm num} - P_\beta(f)_{\rm expt}$. For the statistical analysis we used an ensemble of 5×10^4 realizations.

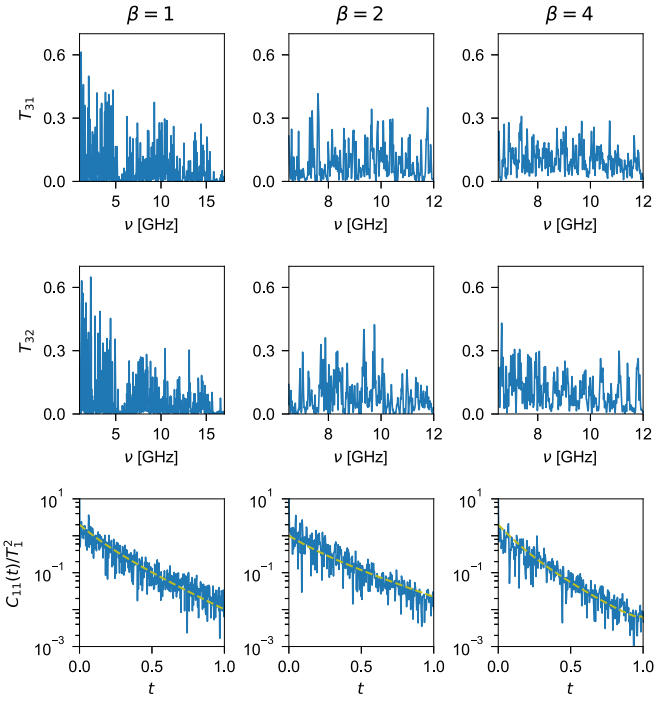

FIG. 5. Experimental transmission intensities T_{31} and T_{32} as a function of frequency are shown in upper and middle panels for the three symmetry classes. The lower panels show the autocorrelation function: the fluctuations are the experimental measurements, and the dashed lines are the best fits of Eq. (27) to the data for $t < 1$.

is extracted from the experimental data as $T_1 = 1 - |\langle S_{11}\rangle|^2$, where $\langle S_{11}\rangle$ is the average (with respect to the frequency) of the scattering matrix element 11. Here we obtained $T_1 = 0.872$ for $\beta = 1$, $T_1 = 0.872$ for $\beta = 2$, and $T_1 = 0.847$ for $\beta = 4$. The effect of dissipation is clearly observed in the experimental transmission intensities T_{31} and T_{32}. Their fluctuations as a function of the frequency are shown in Fig. 5, where we observe that they do not reach the value 1. The dissipation parameter γ can be quantified by fitting the autocorrelation function $C_{11}(t)$ of the 11 element of the scattering matrix [4,28,43]

$$\frac{C_{11}(t)}{T_1^2} = \begin{cases} \left[\frac{3}{(1+2T_1t)^3} - \frac{b_{1,2}(t)}{(1+T_1t)^4}\right]e^{-\gamma t} & \text{for } \beta = 1, \\ \left[\frac{2}{(1+T_1t)^4} - \frac{2^6 b_{2,2}(t)}{(2+T_1t)^6}\right]e^{-\gamma t} & \text{for } \beta = 2, \\ \left[\frac{6}{(1+T_1t)^6} - \frac{2^{12} b_{4,2}(t)}{(2+T_1t)^{10}}\right]e^{-2\gamma t} & \text{for } \beta = 4, \end{cases} \tag{27}$$

where $b_{\beta,2}(t)$ is the two-level form factor [44] and T_1, γ, and t are given in dimensionless units. The best fit achieved for $C_{11}(t)$, for $t < 1$, is shown in Fig. 5 for all symmetry classes, from which we obtain $\gamma = 2.6$ for $\beta = 1$, $\gamma = 2.0$ for $\beta = 2$, and $\gamma = 1.8$ for $\beta = 4$. Note that for the determination of γ the previously determined coupling parameter T_1 are used, and Fig. 5 shows nicely the convergence of the $C_{11}(t = 0)$ to the corresponding values of $2T_1$ for the GOE and GSE cases and T_1 for the GUE. The dips observed for $\beta = 1$ at 5.4 and 16 GHz have their origin in the open-terminated T junctions present in all bonds of the graphs; see Fig. 5. These T junctions had been incorporated to allow for an easy change of the position of the connecting bonds. At the mentioned frequencies standing waves in the short dead end of the T junctions lead to a reduction of the transmission.

Once these parameters are determined, T_1 and γ, RMT simulations can be performed for the scattering matrix of each graph, assumed as quantum systems. In the Heidelberg approach the scattering matrix of a graph can be generated as [9]

$$S_g = 1 - 2\pi i W^\dagger \frac{1}{E - \mathcal{H} + i\pi W W^\dagger} W, \tag{28}$$

where E represents the energy of the incoming wave and W is the matrix that couples the open modes in the ports to the internal modes of the system. $\mathcal{H}$ is an effective Hamiltonian that includes the dissipation γ, $\mathcal{H}_{\mu\nu} = H_{\mu\nu} - i\delta_{\mu\nu}\gamma\Delta/4\pi$, with Δ the mean level spacing. The imperfect coupling can be modeled by adding identical barriers, with transmission intensity T_1, between graph 1 and port 1, between the graphs and the T junction, and between graph 2 and port 2. The numerical simulations of the three-terminal system, with the obtained values of T_1 and γ, lead us to the result shown in Fig. 4 for the distribution of f; see the orange dashed lines in the lower panels. A good agreement is found for the GOE ($\beta = 1$), but for the GUE and GSE we see stronger deviations. In the latter cases only a smaller frequency range was available due to the operating range of the circulators, resulting in a reduced spectral averaging.

V. CONCLUSIONS

Once classical wave systems have been widely shown to be good tools in the description of coherent quantum transport, by means of the conductance in two terminal configurations,

we proposed a three-terminal wave system to indirectly study the voltage drop along a resistor as an alternative transport property. It consists of two microwave graphs to measure the dimensionless voltage drop between the graphs for the three symmetry classes in the Dyson scheme. One port was used as an input, a second port as an exit, and a third port as a probe. The statistical distribution of the quantity f, which accounts for the deviation from the mean value of the potentials in the quantum case, was determined analytically in terms of quadratures that were solved numerically. Also the fluctuations were numerically simulated using the scattering approach of random matrix theory. Qualitatively, we found that the distribution of f is symmetric with respect to zero, which is due to the symmetric configuration of measurement. In this sense, our results extend the ones that were obtained previously for an asymmetric configuration of measurement. Also we found that the shape of the distribution of f is quite similar to the one obtained in the disordered case, in the insulating regime, but with an important difference, which is the effect of weak localization and antilocalization phenomena, not found in the disordered case. Therefore, the effect of the symmetries present in the system is clearly observed in the quantity f, as happens for the conductance in two terminal configurations. A more accurate description is obtained when dissipation and imperfect coupling between the ports and graphs are taken into account. Finally, since the experimental realization of symplectic symmetries is still quite new, there is an interest on its own in a joint study of all symmetry classes. The trouble-free control of the frequency dependence of the quantity f makes the voltage drop an attractive transport property rather than the conductance, which usually requires one to restrict the data analysis to small frequency windows. We expect that our findings could motivate further investigations in the subject.

ACKNOWLEDGMENTS

This work was supported by CONACyT (Grant No. CB-2016/285776). F.C.-R. acknowledges financial support from CONACyT and A.M.M-A. acknowledges support from DGAPA-UNAM. J.A.M.-B. acknowledges financial support from CONACyT (Grant No. A1-S-22706). The experiments were funded by the Deutsche Forschungsgemeinschaft via the individual Grants No. STO 157/17-1 and KU 1525/3-1 including a short-term visit of A.M.M.-A. in Marburg.

APPENDIX A: LIMITS OF INTEGRATION IN Eq. (15)

The integration with respect to $x \in (-1, 1)$ in Eq. (15) should be performed in the interval L, which is the intersection of the intervals $(-1, 1)$ and (α_-, α_+). Since α_+ and α_- depend on the values of τ_1, τ_2, and f, the values of τ_1 and τ_2 may be affected by that intersection for fixed f. This leads to integrals of the form

$$I_a^b(f, \tau_1, \tau_2) = \int_a^b \frac{(A + Bx)\, dx}{\sqrt{(\alpha_+ - x)(x - \alpha_-)(1 + x)(1 - x)}}, \tag{A1}$$

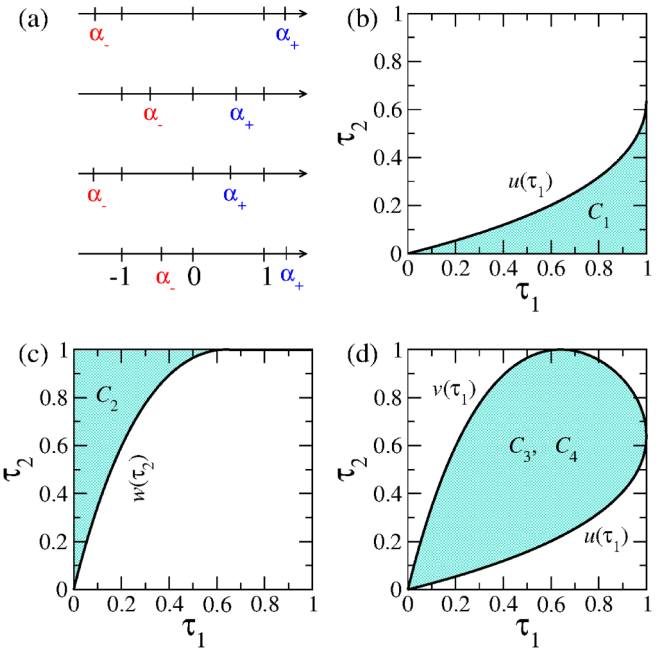

FIG. 6. (a) Intervals of integration for x which imply restrictions on τ_1 and τ_2 (shaded regions): for $|f| = 0.6$ (b) $\tau_2 \in (0, u(\tau_1))$ with $\tau_1 \in (0, 1)$; (c) $\tau_1 \in (0, w(\tau_2))$ with $\tau_2 \in (0, 1)$; (d) $\tau_2 \in (u(\tau_1), v(\tau_1))$ for $f > 0$ and $\tau_2 \in (v(\tau_1), u(\tau_1))$ for $f < 0$, with $\tau_1 \in (0, 1)$. The functions $u(\tau)$, $v(\tau)$, and $w(\tau)$ are defined in Eq. (18).

which gives rise to complete elliptic integrals of the first and third kinds.

Four conditions arise, as illustrated in Fig. 6(a). Restrictions on τ_1 and τ_2 are obtained for a fixed value of f. These restrictions lead to the several regions in the plane $\tau_1 - \tau_2$, as can be seen in Fig. 6.

a. Condition C_1 : $\alpha_- \leqslant -1$ and $1 \leqslant \alpha_+$. Under these conditions x runs over its full domain, $x \in (-1, 1)$. Conditions over α_+ and α_- impose different validity regions for τ_2. Therefore, we take the intersection between such regions and then

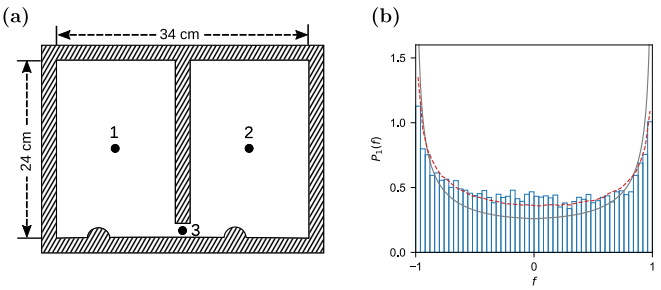

FIG. 7. (a) Sketch of the three-port microwave billiard in the presence of $\beta = 1$ symmetry. The ports are labeled as 1, 2, and 3, where port 3 is used as a probe. The experimental transmission intensities T_{31} and T_{32} are measured between ports 1 and 3, and between ports 2 and 3, respectively. (b) Distribution $P_1(f)$: the continuous (black) line corresponds to the theoretical result shown in Fig. 2, the dashed (red) line is the RMT simulation which takes into account dissipation and imperfect coupling, while the histogram corresponds to the experimental result.

$\tau_2 \in (0, u(\tau_1))$, where $\tau_1 \in (0, 1)$ and $u(\tau_1)$ is given by the first equation in (18).

b. Condition C_2 : $-1 \leqslant \alpha_- \leqslant \alpha_+ \leqslant 1$. For these conditions x belongs to the interval (α_-, α_+) and similarly to condition C_1 we found a restriction over τ_1. Thus, $\tau_1 \in (0, w(\tau_2))$, where $\tau_2 \in (0, 1)$ and $w(\tau_2)$ is given by the third equation in (18).

c. Condition C_3 : $\alpha_- \leqslant -1$ and $-1 \leqslant \alpha_+ \leqslant 1$. In this case x belongs to the interval $(-1, \alpha_+)$. Due to the conditions over α_+ and α_- we have restrictions over τ_1 or τ_2, and we can choose one of them. We choose the restrictions over τ_2 such that $\tau_2 \in (u(\tau_1), v(\tau_1))$ with $f > 0$, where $\tau_1 \in (0, 1)$ and $v(\tau_1)$ is given by the second equation in (18).

d. Condition C_4 : $-1 \leqslant \alpha_- \leqslant 1$ and $1 \leqslant \alpha_+$. Here x belongs to the interval $(\alpha_-, 1)$. Similarly to condition C_3 we choose the restrictions over τ_2 such that $\tau_2 \in (u(\tau_1), v(\tau_1))$ with $f < 0$ and $\tau_1 \in (0, 1)$.

To apply these conditions to the integral of Eq. (A1) we use the equations 254.00, 254.10, 336.01, 336.60, and 340.04 of Ref. [45], and then we integrate with respect to τ_1 and τ_2, and finally we arrive at Eq. (17).

APPENDIX B: THREE-PORT MICROWAVE BILLIARD EXPERIMENT

For the $\beta = 1$ case, in addition to the microwave graph experiments an experiment in a billiard setup has been performed. A sketch is shown in Fig. 7(a). The billiard is constructed on an aluminum plate with two subbilliards of the same shape separated by a central bar. The mirror symmetry is broken by two semicircular obstacles, attached to the bottom boundary. The ports are labeled as 1, 2, and 3, where port 3 is used as a probe. The experimental transmission intensities T_{31} and T_{32} have been measured between port 1 and port 3, and between port 2 and port 3, respectively, for frequencies from 1 to 17 GHz. With a distance of $d = 8$ mm between top and bottom plates the billiard is quasi-two-dimensional in the whole frequency range.

In Fig. 7(b) we show as histogram the experimental distribution of $P_1(f)$ obtained from the billiard setting. The analytical result is shown in the continuous (black) line, while the RMT simulation, which take into account the dissipation and imperfect coupling, is shown in (red) dashed line. Again, a good agreement between experiment and theory is found for $P_1(f)$.

[1] Y. V. Fyodorov, T. Kottos, and H.-J. Stöckmann, Trends in quantum chaotic scattering, J. Phys. A **38**, E01 (2005).

[2] H. Schanze, E. R. P. Alves, C. H. Lewenkopf, and H.-J. Stöckmann, Transmission fluctuations in chaotic microwave billiards with and without time-reversal symmetry, Phys. Rev. E **64**, 065201(R) (2001).

[3] H. Schanze, H.-J. Stöckmann, M. Martínez-Mares, and C. H. Lewenkopf, Universal transport properties of open microwave cavities with and without time-reversal symmetry, Phys. Rev. E **71**, 016223 (2005).

[4] R. Schäfer, T. Gorin, T. H. Seligman, and H.-J. Stöckmann, Correlation functions of scattering matrix elements in microwave cavities with strong absorption, J. Phys. A **36**, 3289 (2003).

[5] U. Kuhl, M. Martínez-Mares, R. A. Méndez-Sánchez, and H.-J. Stöckmann, Direct Processes in Chaotic Microwave Cavities in the Presence of Absorption, Phys. Rev. Lett. **94**, 144101 (2005).

[6] M. Büttiker, Symmetry of electrical conduction, IBM J. Res. Dev. **32**, 317 (1988).

[7] K. Schwab, E. A. Henriksen, J. M. Worlock, and M. L. Roukes, Measurement of the quantum of thermal conductance, Nature (London) **404**, 974 (2000).

[8] M. Büttiker, Y. Imry, and M. Y. Azbel, Quantum oscillations in one-dimensional normal-metal rings, Phys. Rev. A **30**, 1982 (1984).

[9] P. W. Brouwer and C. W. J. Beenakker, Voltage-probe and imaginary-potential models for dephasing in a chaotic quantum dot, Phys. Rev. B **55**, 4695 (1997).

[10] M. W. Keller, A. Mittal, J. W. Sleight, R. G. Wheeler, D. E. Prober, R. N. Sacks, and H. Shtrikmann, Energy-averaged weak localization in chaotic microcavities, Phys. Rev. B **53**, R1693(R) (1996).

[11] C. M. Marcus, A. J. Rimberg, R. M. Westervelt, P. F. Hopkins, and A. C. Gossard, Conductance Fluctuations and Chaotic Scattering in Ballistic Microstructures, Phys. Rev. Lett. **69**, 506 (1992).

[12] I. H. Chan, R. M. Clarke, C. M. Marcus, K. Campman, and A. C. Gossard, Ballistic Conductance Fluctuations in Shape Space, Phys. Rev. Lett. **74**, 3876 (1995).

[13] M. Martínez-Mares, Statistical fluctuations of the parametric derivative of the transmission and reflection coefficients in absorbing chaotic cavities, Phys. Rev. E **72**, 036202 (2005).

[14] E. Flores-Olmedo, A. M. Martínez-Argüello, M. Martínez-Mares, G. Báez, J. A. Franco-Villafañe, and R. A. Méndez-Sánchez, Experimental evidence of coherent transport, Sci. Rep. **6**, 25157 (2016).

[15] M. Büttiker, Four-Terminal Phase-Coherent Conductance, Phys. Rev. Lett. **57**, 1761 (1986).

[16] V. A. Gopar, M. Martínez, and P. A. Mello, Random-matrix study of multiprobe mesoscopic devices. II. A four-probe one-dimensional system, Phys. Rev. B **50**, 2502 (1994).

[17] L. Arrachea, C. Naón, and M. Salvay, Voltage profile and four-terminal resistance of an interacting quantum wire, Phys. Rev. B **77**, 233105 (2008).

[18] C. Texier and G. Montambaux, Four-terminal resistances in mesoscopic networks of metallic wires: Weak localisation and correlations, Physica E **82**, 272 (2016).

[19] F. Foieri, L. Arrachea, and M. J. Sánchez, dc four-point resistance of a double-barrier quantum pump, Phys. Rev. B **79**, 085430 (2009).

[20] J. L. D'Amato and H. M. Pastawski, Conductance of a disordered linear chain including inelastic scattering events, Phys. Rev. B **41**, 7411 (1990).

[21] C. J. Cattena, L. J. Fernández-Alcázar, R. A. Bustos-Marún, D. Nozaki, and H. M Pastawski, Generalized multi-terminal decoherent transport: Recursive algorithms and applications to SASER and giant magnetoresistance, J. Phys. C **26**, 345304 (2014).

[22] A. M. Song, A. Lorke, A. Kriele, J. P. Kotthaus, W. Wegscheider, and M. Bichler, Nonlinear Electron Transport in an Asymmetric Microjunction: A Ballistic Rectifier, Phys. Rev. Lett. **80**, 3831 (1998).

[23] B. Gao, Y. F. Chen, M. S. Fuhrer, D. C. Glattli, and A. Bachtold, Four-Point Resistance of Individual Single-Wall Carbon Nanotubes, Phys. Rev. Lett. **95**, 196802 (2005).

[24] A. M. Martínez-Argüello, J. A. Méndez-Bermúdez, and M. Martínez-Mares, Phenomenological approach to transport through three-terminal disordered wires, Phys. Rev. E **99**, 062202 (2019).

[25] S. Godoy and P. A. Mello, The voltage drop along a mesoscopic conductor. Is it a well-defined macroscopic variable? Are there limitations in its determination? Europhys. Lett. **17**, 243 (1992).

[26] S. Godoy and P. A. Mello, Random-matrix study of multiprobe mesoscopic devices: A three-probe one-dimensional system, Phys. Rev. B **46**, 2346 (1992).

[27] A. M. Martínez-Argüello, E. Castaño, and M. Martínez-Mares, Random matrix study for a three-terminal chaotic device, AIP Conf. Proc. **1579**, 46 (2014).

[28] A. M. Martínez-Argüello, A. Rehemanjiang, M. Martínez-Mares, J. A. Méndez-Bermúdez, H.-J. Stöckmann, and U. Kuhl, Transport studies in three-terminal microwave graphs with orthogonal, unitary, and symplectic symmetry, Phys. Rev. B **98**, 075311 (2018).

[29] M. A. Heald and J. B. Marion, *Classical Electromagnetic Radiation*, 3rd ed. (Saunders College Publishing, Fort Worth, TX, 1995).

[30] C. W. J. Beenakker, Random-matrix theory of quantum transport, Rev. Mod. Phys. **69**, 731 (1997).

[31] K. Życzkowski, Random matrices of circular symplectic ensemble, in *Chaos—The Interplay between Stochastic and Deterministic Behaviour,* Lecture Notes in Physics, edited by P. Garbaczewski, M. Wolf, and A. Weron (Springer, Berlin, 1995), Vol. 457, pp. 565–571.

[32] A. Rehemanjiang, M. Richter, U. Kuhl, and H.-J. Stöckmann, Spectra and spectral correlations of microwave graphs with symplectic symmetry, Phys. Rev. E **97**, 022204 (2018).

[33] A. Rehemanjiang, M. Allgaier, C. H. Joyner, S. Müller, M. Sieber, U. Kuhl, and H.-J. Stöckmann, Microwave Realization of the Gaussian Symplectic Ensemble, Phys. Rev. Lett. **117**, 064101 (2016).

[34] T. Kottos and U. Smilansky, Quantum Chaos on Graphs, Phys. Rev. Lett. **79**, 4794 (1997).

[35] T. Kottos and U. Smilansky, Periodic orbit theory and spectral statistics for quantum graphs, Ann. Phys. (NY) **274**, 76 (1999).

[36] T. Kottos and U. Smilansky, Quantum graphs: A simple model for chaotic scattering, J. Phys. A **36**, 3501 (2003).

[37] S. Gnutzmann and A. Altland, Universal Spectral Statistics in Quantum Graphs, Phys. Rev. Lett. **93**, 194101 (2004).

[38] O. Hul, S. Bauch, P. Pakoñski, N. Savytskyy, K. Życzkowski, and L. Sirko, Experimental simulation of quantum graphs by microwave networks, Phys. Rev. E **69**, 056205 (2004).

[39] M. Ławniczak, O. Hul, S. Bauch, P. Šeba, and L. Sirko, Experimental and numerical investigation of the reflection coefficient and the distributions of Wigner's reaction matrix for irregular graphs with absorption, Phys. Rev. E **77**, 056210 (2008).

[40] M. Ławniczak, S. Bauch, O. Hul, and L. Sirko, Experimental investigation of the enhancement factor for microwave irregular networks with preserved and broken time reversal symmetry in the presence of absorption, Phys. Rev. E **81**, 046204 (2010).

[41] M. Ławniczak, B. van Tiggelen, and L. Sirko, Experimental investigation of distributions of the off-diagonal elements of the scattering matrix and Wigner's $\hat{K}$ matrix for networks with broken time reversal invariance, Phys. Rev. E **102**, 052214 (2020).

[42] B. Dietz, V. Yunko, M. Białous, S. Bauch, M. Ławniczak, and L. Sirko, Nonuniversality in the spectral properties of time-reversal-invariant microwave networks and quantum graphs, Phys. Rev. E **95**, 052202 (2017).

[43] Y. V. Fyodorov, D. V. Savin, and H.-J. Sommers, Scattering, reflection and impedance of waves in chaotic and disordered systems with absorption, J. Phys. A **38**, 10731 (2005).

[44] T. Guhr, A. Müller-Groeling, and H. A. Weidenmüller, Random matrix theories in quantum physics: Common concepts, Phys. Rep. **299**, 189 (1998).

[45] P. F. Byrd and M. D. Friedman, *Handbook of Elliptic Integrals for Engineers and Physicists*, Grundlehren der Mathematischen Wissenschaften (Springer-Verlag, Berlin, 1954), Vol. 67.